Jordan Journal of Civil Engineering, Volume **20**, No. **4**, **2026**
DOI: https://doi.org/10.14525/JJCE.v20i4.05

Jordan Journal of Civil Engineering

Journal homepage: https://jjce.just.edu.jo

Application of Improved FBG Sensor in Monitoring Dynamic Strain and Shear Deformation of Geotechnical Engineering

Chao Jia[1)*], Haiyang Shen [1)], Jining Zhang [2)]

[1)] *College of Architectural Engineering, Shanxi Vocational University of Engineering Science and Technology, Jinzhong, 030619, China. * Corresponding Author. Email: jiachao198901@163.com*
[2)] *Shanxi Metallurgical Geotechnical Engineering Exploration Co., Ltd., Taiyuan, 030002, China.*

ARTICLE INFO

Article History:
Received: 11/3/2026
Accepted: 8/6/2026

ABSTRACT

In geotechnical engineering, stress parameter monitoring is constrained by complex environments, posing challenges to traditional single-point monitoring techniques. To enhance dynamic monitoring of geotechnical strain and shear deformation, this study proposes a sensor based on improved fiber Bragg grating. The research first demodulates the sensors, and optimizes the monitoring system. Subsequently, the study combines the dual-grating compensation method to eliminate temperature interference and optimizes the strain offset step size through an improved convolutional neural network. In the calibration experiment, the sensor demonstrated a fitting coefficient of 0.998 between wavelength shift and temperature, indicating excellent stability. During the loading experiment, the sensitivities of Sensor 3 and Sensor 4 were 12.472nm/mm and 12.468nm/mm, respectively, meeting the precision requirements. Additionally, in geotechnical dynamic strain monitoring, the research sensor achieved a monitoring error controlled within 7.8με, outperforming traditional sensors. In shear deformation monitoring, the optimized sensor had a maximum monitoring error of 0.47mm, which was superior to traditional sensors. The improved fiber Bragg grating sensor has excellent application effects in the field of geotechnical detection. This study will provide technical support for structural deformation and environmental monitoring in geotechnical engineering.

Keywords: FBG, Geotechnical engineering, Strain, Monitoring, Grating compensation method; Convolutional neural network.

INTRODUCTION

Fiber Bragg Grating (FBG) sensor is a high-precision sensing technology based on the principle of fiber grating (Kok et al., 2024). It uses the Bragg grating in optical fibers to detect physical quantities, such as temperature, strain, pressure, … etc. by detecting changes in the reflection characteristics of light (Zhao et al., 2023). FBG sensors have anti-electromagnetic interference, high sensitivity, and easy remote monitoring, and are widely used in civil engineering, aerospace, medical, and other fields (Li et al., 2024). Compared with conventional tools, such as vibrating wire sensors and resistive strain gauges, FBG is selected for its superior reliability in complex environments. While traditional electrical sensors are often susceptible to electromagnetic interference and moisture-induced corrosion, FBG provides higher resolution, immunity to electromagnetic noise, and excellent multiplexing capabilities for large-scale geotechnical monitoring.

In recent years, relevant research has been continuously deepened, and numerous studies have conducted detailed discussions on its performance optimization and application expansion. Alias et al. conducted research on the difficulty of ensuring high-resolution, accurate, and high-sensitivity sensing of FBG sensors in complex environments. A diversified sensor design technology based on FBGs was proposed. This technology designed different types of FBG sensors, such as phase grating FBG, which used grating packaging to improve sensitivity and achieved precise sensing through refractive index changes and peak tracking methods. The results indicated that the sensor had effective application effects in various scenarios (Alias et al., 2024). Prathap and Saara conducted research on the performance optimization of FBG weighing sensors and proposed a novel FBG weighing sensor based on 3D printing technology. This technology explored the effects of adjusting the filling density and pattern on the temperature and mechanical strain sensitivity of FBGs. Two FBGs used for strain measurement and temperature compensation, respectively. The results indicated that this technology had sensitivity and monitoring accuracy, which were superior to those of traditional FBG sensors (Prathap & Saara, 2024). Zhang et al. proposed a novel FBG 3D printed geogrid technology to address the road construction in karst areas. This technology combined the advantages of geosynthetic materials and FBG, and achieved complete coordinated deformation between FBG sensors and geogrids through 3D printing technology. A series of model experiments were conducted. The results showed that this technology had excellent performance in road pressure and stress monitoring, and had high detection stability (Zhang et al., 2023).

In the field of geotechnical strain monitoring, FBG sensors have demonstrated unique advantages. Their high precision and anti-interference characteristics can accurately capture small strain changes in rock and soil, providing reliable data for engineering safety warning. Han et al. conducted research on the real-time monitoring of landslide shear displacement and proposed a strain sensing optical cable based on ultra weak FBG technology. This technology designed an optical cable and proposed two calculation models to convert cable strain into shear displacement. This technology had excellent performance in geotechnical testing in the Three Gorges Reservoir area, and could effectively monitor regional landslides and strains (Han et al., 2023). Shaw et al. monitored shear deformation in sliding zones in geotechnical engineering, conducted direct shear model experiments, captured internal soil deformation using FBG, and measured soil surface deformation using particle image velocimetry to obtain strain related data. This technology was suitable for monitoring different types of rock and soil and complex working conditions, and performed excellently (Wang et al., 2024). Sun et al. conducted research on the difficulty of monitoring the moisture content of deep soil in geotechnical engineering and proposed a new type of active heating FBG cable. This technology evaluated heating uniformity through laboratory testing, established a temperature characteristic value soil moisture calibration equation, and conducted on-site monitoring in a test pit on the Loess Plateau. The results indicated that the proposed technology could effectively monitor soil water content and dynamically monitor rock and soil strain (Sun et al., 2025). Hu et al. monitored soil infiltration pressure in geotechnical engineering and developed a sensor that combined corrugated membrane and FBG. Through soil seepage monitoring tests and laboratory slope model tests, the results showed that this technology had stability and accuracy, meeting the requirements for long-term stability monitoring of rock and soil (Hu et al., 2023).

According to the above research, FBG sensors have been applied in many fields, such as healthcare, geotechnical engineering, and construction. This sensor is based on the principle that the wavelength of light reflected by a grating varies with stress, and has advantages, such as small size, resistance to electromagnetic interference, and ease of networking. It has shown great potential in geotechnical monitoring (Karkush & Ali, 2025). However, traditional FBG sensors also have shortcomings, such as poor long-term stability in complex geotechnical environments, inadequate temperature compensation mechanisms, and susceptibility to complex environmental interference (Choi et al., 2024). To overcome these limitations, an improved FBG sensor is proposed and applied in the field of dynamic strain and shear deformation monitoring of rock and soil. While conventional FBG modeling and CNN optimizations are established, the research integrates a segmented transfer matrix method for non-uniform grid spacing with a spatial attention-enhanced CNN. This specific combination addresses the nonlinear strain-spatial offset relationship unique to complex geotechnical surfaces, distinguishing it from incremental individual improvements.

There are two innovations in the research. One is to construct an FBG sensor model based on coupling mode theory, analyze the spectral characteristics of non-uniform grid spacing FBG using segmented transfer matrix method, and establish an improved FBG sensor monitoring system. The second is to introduce the improved Convolutional Neural Network (CNN) combined with an attention mechanism, adjust the sensitivity of sensors to local deformation of rock and soil, and improve monitoring accuracy in complex environments. The research content will provide technical support for the safe construction and monitoring of geotechnical engineering. The research establishes a meaningful connection to geotechnical engineering by demonstrating how the spatial attention-enhanced FBG sensors capture localized nonlinear deformation and rapid shear failure in soil mass, providing higher fidelity data than conventional tools for dynamic stability evaluation.

RESEARCH DESIGN

Modeling and Demodulation Optimization of FBG Sensors

In the field of geotechnical engineering, the monitoring of parameters related to geotechnical stress is affected by complex environments and faces challenges on monitoring range and accuracy (Dostovalov et al., 2024). FBG sensors, with their advantages of small size, strong anti-interference ability, and high sensitivity, have been widely used in the field of geotechnical engineering (Karkus et al., 2020). An FBG sensor model based on coupling mode theory is used for dynamic monitoring of stress and shear deformation in geotechnical scenarios. The schematic diagram of FBG sensor structure is shown in Figure 1.

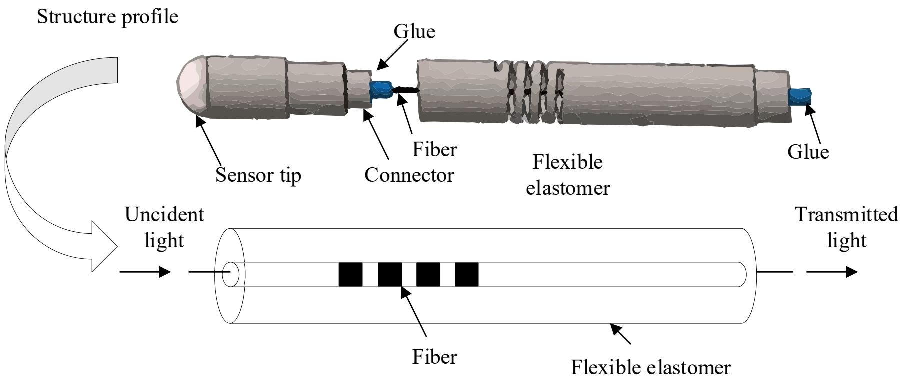

Figure 1. FBG sensor frame structure

From Figure 1, the FBG sensor consists of three key parts: grating, core, and cladding. Its principle is to reflect external strain through changes in grating period and effective refractive index of the core. The research technology process includes three parts: designing FBG structures based on coupling mode theory, analyzing optical propagation characteristics, and extracting demodulation methods, to establish a quantitative relationship between strain and center wavelength shift, providing a foundation for subsequent geotechnical monitoring. In Figure 1, when broadband light is incident, specific wavelength light that satisfies the Bragg condition is reflected. The reflection center wavelength λ_B is represented by Equation (1) (Yamaguchi et al., 2023).

$$\lambda_B = 2n_{\text{eff}}\Lambda \tag{1}$$

In Equation (1), n_{eff} is the effective refractive index of the fiber core. Λ is the grating period. When the sensor is subjected to strain, n_{eff} and Λ change, and Λ shifts. The research characterizes the Bragg condition based on the phase-matching requirement, where constructive interference occurs when reflected waves from periodic modulations are in phase. The shift in λ_B due to temperature fluctuations is theoretically determined by the coupled effects of thermal expansion and thermo-optic modulation. This behavior is described by the Equation $\Delta\lambda_B = \lambda_B(\alpha_\Lambda + \xi_n)\Delta T$, where α_Λ and ξ_n denote the thermal expansion and thermo-optic coefficients, respectively. The research interprets the observed increase in λ_B as a result of the increase in

n_{eff} and the physical elongation of Λ caused by rising temperatures.

By monitoring the offset, the magnitude of the strain can be inverted. In addition, the strain represents the ratio of material deformation to original length, as calculated in Equation (2) (Karkush et al., 2022).

$$\varepsilon = \lim_{L \to 0} \frac{\Delta L}{L} \tag{2}$$

In Equation (2), ε is the strain. L is the original length of the material. ΔL is the amount of deformation. When FBG is subjected to axial strain, the grating period changes by $\Delta\Lambda = \Lambda\varepsilon$, and the elastic optical effect causes a change in n_{eff}. The relationship between the final center wavelength shift $\Delta\lambda_B$ and strain is shown in Equation (3) (Chen et al., 2024).

$$\Delta\lambda_B = \lambda_B (1 - P_\varepsilon)\varepsilon \tag{3}$$

In Equation (3), P_ε is the effective elastic optical coefficient, which is designed using quartz fiber, with a value of 0.2. The linear relationship between strain and wavelength shift is established through Equation (3), which is the theoretical basis for FBG strain monitoring. In addition, the coupled mode theory derived from Maxwell's equations is the core tool for analyzing the internal light propagation of FBGs in geotechnical engineering analysis (Adibania et al., 2023). After ignoring the time factor, the wave equation of the optical field in the fiber is shown in Equation (4) (Al-Mamoori et al., 2025).

$$\nabla^2 \mathbf{E} + k_0^2 n^2 \mathbf{E} + \nabla\left(\mathbf{E} \cdot \frac{\nabla\varepsilon}{\varepsilon}\right) = 0 \tag{4}$$

In Equation (4), k_0 is the wave number in vacuum. **E** is the electric field strength. n is the refractive index. After simplification through weak guidance approximation, the optical field can be represented as a superposition of guided modes propagating along the axial direction of the fiber, and its coupled mode equations are shown in Equation (5) (Ioannau & Kalli, 2023).

$$\begin{cases} \dfrac{dA_\mu}{dz} = i\sum_\nu A_\nu (k^t + k^z)\exp\left[i(\beta_\nu - \beta_\mu)z\right] + i\sum_\nu B_\nu (k^t - k^z)\exp\left[-i(\beta_\nu + \beta_\mu)z\right] \\ \dfrac{dB_\mu}{dz} = -i\sum_\nu A_\nu (k^t - k^z)\exp\left[i(\beta_\nu + \beta_\mu)z\right] - i\sum_\nu B_\nu (k^t + k^z)\exp\left[-i(\beta_\nu - \beta_\mu)z\right] \end{cases} \tag{5}$$

In Equation (5), A_μ and B_μ are the mode amplitudes propagating along the ±z direction, respectively. β is the propagation constant. k^t and k^z are the transverse and longitudinal coupling coefficients. The research utilizes these equations to quantify the energy transfer between counter-propagating modes, with the coupling intensity determined by the refractive index perturbation within the fiber core. In addition, for non-uniform grid spacing, the segmented transmission matrix method is used to analyze its spectral characteristics. The grating is divided into m segments. The transmission characteristics of each segment are represented by an 2×2 matrix, as shown in Equation (6).

$$\begin{pmatrix} R_i \\ S_i \end{pmatrix} = F_i \begin{pmatrix} R_{i+1} \\ S_{i+1} \end{pmatrix} \tag{6}$$

In Equation (6), R_i and S_i represent the backward and forward wave amplitudes of the i-th segment. F_i is the transmission matrix. The research determines the total spectral response by cascading the transmission matrices of discrete segments, effectively accounting for the phase accumulation and field coupling across the non-uniform FBG structure. By matrix multiplication, the overall transmission characteristics can be obtained, which can accurately control the peak, half width, and sidelobes of the echo spectrum, and optimize the signal quality of FBG in geotechnical monitoring. The mathematical demonstration of the improved FBG model is grounded in the segmented transfer matrix theory, which characterizes non-uniform gratings by discretizing the fiber into N homogeneous sections. By multiplying the transmission matrices of these sections, the total spectral response is synthesized, allowing the research to rigorously account for local perturbations in the effective refractive index and grating period caused by complex geotechnical stress.

In addition, according to the principle of FBG sensors, they can directly measure parameters, such as strain and temperature of soil and rock. Based on the distributed multi-point control, the accuracy of soil and rock monitoring can be significantly improved. However, this process requires high-precision demodulation for the FBG center wavelength to ensure monitoring accuracy. The study adopts the laser wavelength matching demodulation method, and the technical principle is shown in Figure 2.

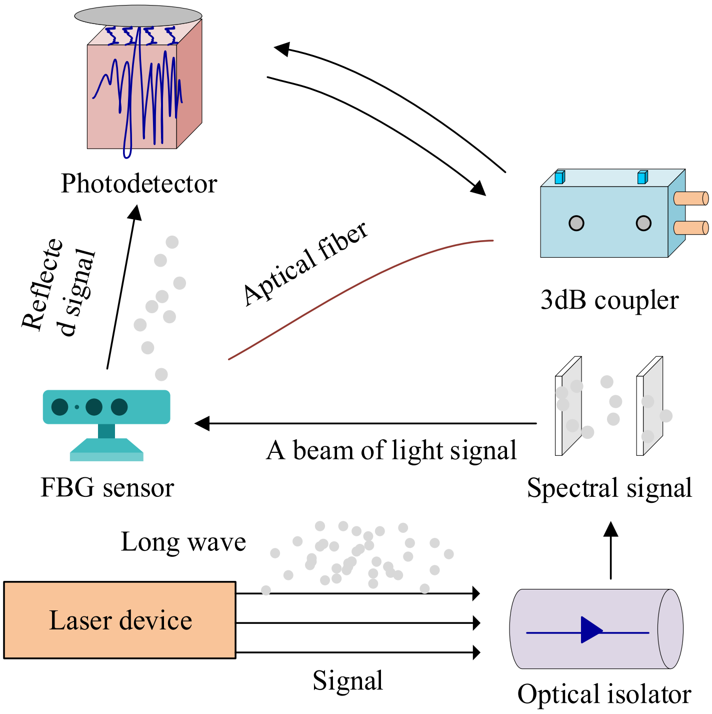

Figure 2. Principle of laser wavelength matching demodulation (https://www.svgrepo.com/vectors/sensor/)

According to Figure 2, the principle is to adjust the laser wavelength to match the FBG reflection peak, and identify the wavelength corresponding to the maximum light intensity through a photodetector, which is suitable for monitoring the strain in dynamic geotechnical engineering scenes. In addition, considering that temperature changes can cause wavelength shift of FBGs, the study adopts the dual-grating compensation method for optimization, that is, two FBGs with different center wavelengths are symmetrically pasted on both sides of the rock and soil mass. The wavelength shift caused by temperature is the same, while the shift direction caused by strain is opposite. The relationship between the change in center wavelength shift is shown in equation (7) (Abdulraheem et al., 2024).

$$\Delta\lambda_{B2} - \Delta\lambda_{B1} = 2K_{\varepsilon}\Delta\varepsilon \tag{7}$$

In Equation (7), $\Delta\lambda_{B2}$ and $\Delta\lambda_{B1}$ are the two center wavelength offsets. K_{ε} is the strain sensitivity coefficient. $\Delta\varepsilon$ is the strain offset. Based on this equation, temperature interference can be eliminated and strain signals can be effectively extracted.

Design of Strain Force Monitoring System for Complex Geotechnical Surfaces

In the specific application of FBG sensors in rock and soil, complex rock and soil surfaces have characteristics, such as nonlinear curvature and multiple crack distribution. Traditional FBG sensors for single point monitoring are difficult to capture changes in the global strain field, which can easily lead to missed key deformation information. On the basis of FBG adjustment technology, an improved FBG sensor monitoring system for complex rock and soil surfaces is proposed to monitor rock and soil. The system framework is shown in Figure 3.

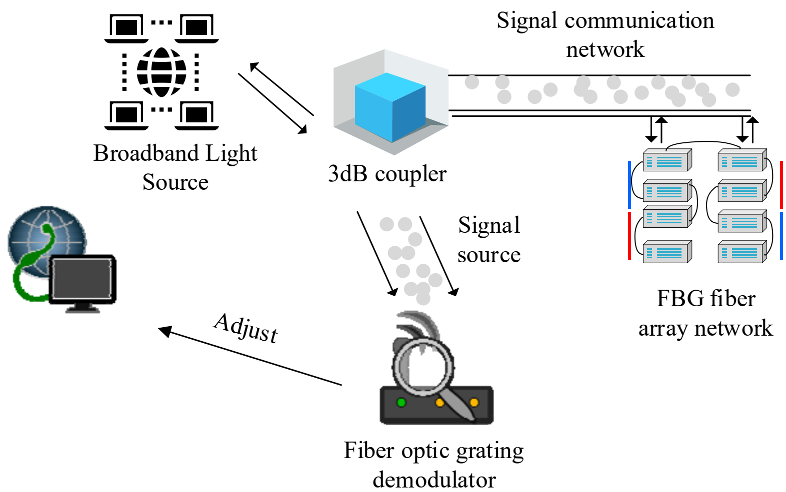

Figure 3. Improved FBG sensor monitoring framework (https://www.svgrepo.com/vectors/machine/2; https://www.svgrepo.com/vectors/broadband/2)

According to Figure 3, the system includes broadband light source, FBG sensing array, fiber coupler, demodulator, and upper computer. The follow-up research work mainly includes selecting core components that are suitable for geotechnical environments, optimizing sensor network layout based on finite element simulation, and establishing the mathematical relationship between strain and spatial offset involves three processes. Firstly, it is necessary to select core components suitable for the geotechnical environment. Based on the key components in Figure 3, a tunable laser light source is selected for design, and a GM8050 demodulator with a demodulation accuracy of 0.1pm and 4 channels is used in the system to ensure high fidelity acquisition of dynamic strain signals. In the FBG sensors, a coding modulation method for FBG echo spectrum control is used to optimize the echo spectrum and improve the recognition ability of weak strain and shear deformation in rock and soil (Salman et al., 2024). The grating is divided into m segments along the axis. The transmission characteristic of each segment is represented by a matrix, as shown in Equation (8).

$$\begin{pmatrix} R_i \\ S_i \end{pmatrix} = F_i \begin{pmatrix} R_{i+1} \\ S_{i+1} \end{pmatrix} \tag{8}$$

In Equation (8), R_i and S_i represent the backward and forward wave amplitudes of the i-th segment, respectively. F_i is the transmission matrix. The number of segments must meet the requirements, as shown in Equation (9) (Gul & Ahmad, 2022).

$$m \square \frac{2n_{\text{eff}}L}{\lambda_B} \tag{9}$$

In Equation (9), λ_B is the center wavelength. In addition, to cover the complex surface strain field of rock and soil, ANSYS simulation is used to analyze the strain distribution characteristics and optimize the sensor layout accordingly. The curvature sequence of the rock and soil surface is set as k_1, k_2, …, k_n. The curvature of the first sensor deployment position is shown in Equation (10).

$$k_{m1} = \frac{k_n - k_1}{m} \tag{10}$$

The subsequent position is determined by the recursive equation $k_{m2} = k_{m1} + \frac{k_n - k_1}{m}$ o capture the area of sudden changes in the curvature of the rock and soil surface. In addition, for areas with large curvature of rock and soil, an axial "|" shape is used to monitor axial strain. For areas with gentle curvature, an orthogonal "-" shape is used to synchronously monitor radial strain. In addition, to accurately monitor the strain and shear deformation of rock and soil masses, a strain and spatial offset model is constructed. In this process, if the wavelength offset of six FBGs is $\Delta\lambda_{B1}$~$\Delta\lambda_{B6}$, the three-dimensional offset component is shown in Equation (11).

$$\begin{cases} dx = (\Delta\lambda_{B1} \cdots \Delta\lambda_{B6}) \cdot \begin{pmatrix} C_{x1} \\ \vdots \\ C_{x6} \end{pmatrix} \\ dy = (\Delta\lambda_{B1} \cdots \Delta\lambda_{B6}) \cdot \begin{pmatrix} C_{y1} \\ \vdots \\ C_{y6} \end{pmatrix} \\ dz = (\Delta\lambda_{B1} \cdots \Delta\lambda_{B6}) \cdot \begin{pmatrix} C_{z1} \\ \vdots \\ C_{z6} \end{pmatrix} \end{cases} \tag{11}$$

In Equation (11), C_{x1}~C_{z6} are calibration coefficients. *dx*, *dy*, and *dz* are the offsets in the X, Y, and Z directions. The shear deformation offset is shown in Equation (12).

$$D = \sqrt{dx^2 + dy^2 + dz^2} \tag{12}$$

Through the above analysis, various parameters of rock and soil can be accurately and effectively monitored, and the monitoring effect of FBG sensors on complex rock and soil surfaces can be improved.

Optimization of Strain Offset Step Size Based on Improved CNN

Although the improved FBG sensor monitoring system can adapt to most geotechnical scenarios, in environments with abnormal temperature and humidity, the nonlinear relationship between strain and spatial offset can lead to insufficient accuracy of traditional mathematical models, especially in areas with significant shear deformation, resulting in increased monitoring errors. Recent reference on FBG and machine learning integration often overlooks the complex nonlinear coupling effects under abnormal conditions. The research fills this gap using the attention mechanism to dynamically adjust feature weights in significant shear deformation areas, advancing beyond standard machine learning applications in geotechnical monitoring. The study introduces an improved CNN to optimize the problem. The technical process is shown in Figure 4.

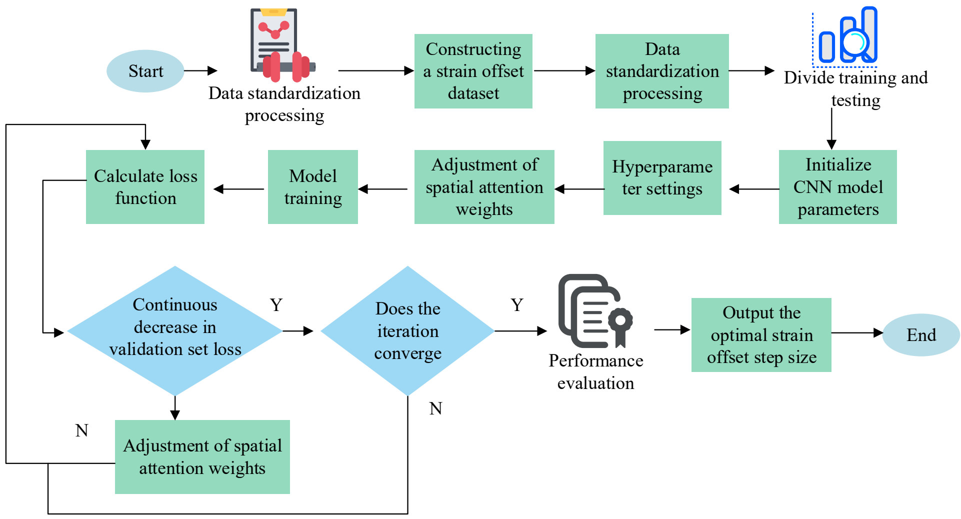

Figure 4. Optimization process of strain offset step size based on improved CNN (https://www.svgrepo.com/vectors/training/; https://www.svgrepo.com/vectors/data/; https://www.svgrepo.com/vectors/evaluate/)

According to Figure 4, the improved FBG sensor adopts an improved CNN combined with attention mechanism to adjust the sensitivity of the sensor to local deformation of rock and soil. The process includes constructing a strain-offset sample dataset, designing a deep learning model with attention module, and parameter optimization. In constructing a strain-offset sample dataset, the study uses strain data $\varepsilon_1 \sim \varepsilon_6$ from six FBG sensors on the surface of rock and soil as input features, and the spatial offset *D* measured by a visual detection system as labels to construct the sample dataset. During the data collection process, 1,000 sets of samples are generated by changing the stress load and action point of the rock and soil mass, of which 800 sets are used for training and 200 sets are used for testing. To enhance feature representativeness, the original strain data is standardized to eliminate interference from strain data of different magnitudes, as shown in Equation (13) (Liu et al., 2022).

$$\hat{\varepsilon}_i = \frac{\varepsilon_i - \mu_\varepsilon}{\sigma_\varepsilon} \tag{13}$$

In Equation (13), μ_ε is the mean strain. σ_ε is the standard deviation of strain. $\hat{\varepsilon}_i$ is the standardized strain value. In addition, to enhance the feature weights of the deformation sensitive areas of the rock and soil mass, a spatial attention module is introduced into the CNN. The CNN is improved, as shown in Figure 5.

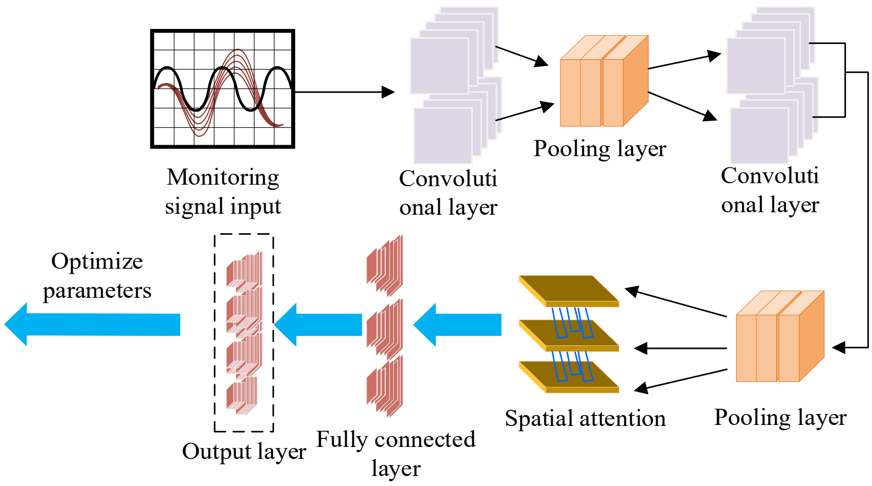

Figure 5. Improved CNN structure diagram

According to Figure 5, the model includes components, such as convolution and pooling. The CNN input layer receives a 6-dimensional strain feature vector $\hat{\varepsilon}_1 \sim \hat{\varepsilon}_6$, while the convolutional layer uses a 3×3 convolution kernel to map the input features, as shown in Equation (14) (Presti et al., 2023).

$$X_{i,j}^{l} = \sum_{m=1}^{3}\sum_{n=1}^{3} X_{m,n}^{l-1} \cdot W_{i-m+1,\,j-n+1}^{l} + b^{l} \tag{14}$$

In Equation (14), $X_{i,j}^{l}$ is the convolution output of the l-th layer. W^l is the convolution kernel weight. b^l is the bias term. Local correlation information of strain features can be extracted through this layer. Subsequently, the model generates attention weights through the Sigmoid function, as shown in Equation (15).

$$A_{i,j} = \sigma\left(\sum_{k=1}^{C} X_{i,j,k} \cdot W_k + b_A\right) \tag{15}$$

In Equation (15), σ is the Sigmoid activation function. C is the number of feature channels. W_k is the attention weight. $A_{i,j}$ is the spatial attention coefficient. The weight adjustment can be used to enhance the feature weights of significant areas of rock and soil shear deformation (Hebbi & Mamatha, 2023). Finally, the spatial offset prediction value $\hat{D}$ is output through the fully connected layer. In addition, the model training uses the Mean Squared Error (MSE) loss function to optimize the model performance, as shown in Equation (16).

$$L = \frac{1}{N}\sum_{k=1}^{N}(\hat{D}_k - D_k)^2 \tag{16}$$

In Equation (16), N represents the number of samples. $\hat{D}_k$ is the predicted offset. D_k is the actual offset. The model parameters are optimized through gradient descent method.

RESULTS

FBG Sensor Calibration Experiment

To effectively evaluate the application effect of the improved FBG sensor in geotechnical scenes, the study conducts FBG sensor calibration experiments and geotechnical scene strain and shear deformation monitoring experiments. The software and hardware parameter information is shown in Table 1.

Table 1. Experimental software and hardware environment information

Project	Parameter
Demodulation system	GM8050 fiber Bragg grating demodulator
Loading device	Direct cutting instrument, temperature control box
Data collection tool	Modbus protocol tool
Visualization tool	ZedGraph and VXelements software
Experimental system	WINDOWS 11
Processor	INTEL i7 12700
Graphics card	RTX 3070
Memory	64G

According to Table 1, the study uses GM8050 as the FBG demodulator for the FBG sensor system, with a wavelength range of 1,527-1,568nm, a sampling frequency of 20Hz, and a demodulation accuracy of 0.1pm. The architecture of the improved CNN is configured with an input layer, two convolutional layers, one max-pooling layer, the spatial attention module, and two fully connected layers. The training process is executed using the Adam optimizer, with a learning rate of 0.001, a batch size of 32, and 150 epochs to ensure model convergence. In addition, a direct shear apparatus is used to assist in the experiment, and temperature sensors are used to monitor the ambient temperature. The lithologic sandy soil in Dujiangyan Irrigation Project mountainous area is collected as the experimental material for rock and soil monitoring. The specific gravity of the soil particles is 2.67, the dry density is 1.6/cm^3, the maximum void ratio is 0.579, the non-uniformity coefficient is 1.61, and the maximum void ratio is 0.878. The specific experimental process involves making the sample into a 500mm×250mm×350mm test sample and conducting experimental testing with a controlled moisture content of 5%. To ensure calibration clarity, the sand specimen is prepared using a layer-by-layer tamping technique to achieve uniform density. The FBG sensors are embedded with a specialized coupling interface to ensure synchronized deformation with the soil skeleton to accurately correlate optical signals with the dynamic mechanical behavior of the material. Before conducting the experiment, sensitivity analysis is conducted on key FBG parameters to determine baseline performance at different grating lengths. The sensitivity results of temperature and strain are shown in Table 2.

Table 2. Sensitivity analysis of key FBG parameters

Grating Length (mm)	Temperature Range (℃)	Strain Range (με)	Temperature Sensitivity (pm/℃C)	Strain Sensitivity (pm/με)
10	0-100	0-2000	10.42	1.20
15	0-100	0-2000	10.51	1.22
20	0-100	0-2000	10.48	1.21

Based on the data in Table 2, the grating length had a minimal effect on the sensitivity coefficients, stabilizing at approximately 10.5 pm/°C for temperature and 1.21 pm/με for strain. This confirms that the effective refractive index change dominates the wavelength shift, providing a highly stable theoretical basis for subsequent geotechnical monitoring.

Firstly, a temperature calibration experiment is conducted by placing four sets of FBG sensors into a prepared temperature control box. The sensors are connected and debugged using a FBG demodulation device and an optical fiber. The temperature inside the adjustment box is set within the range of -20℃ to 100℃, that is, the temperature is raised from the lowest to the maximum at a rate of 1℃/min. The center wavelength data of the FBG is collected. The test results are shown in Figure 6.

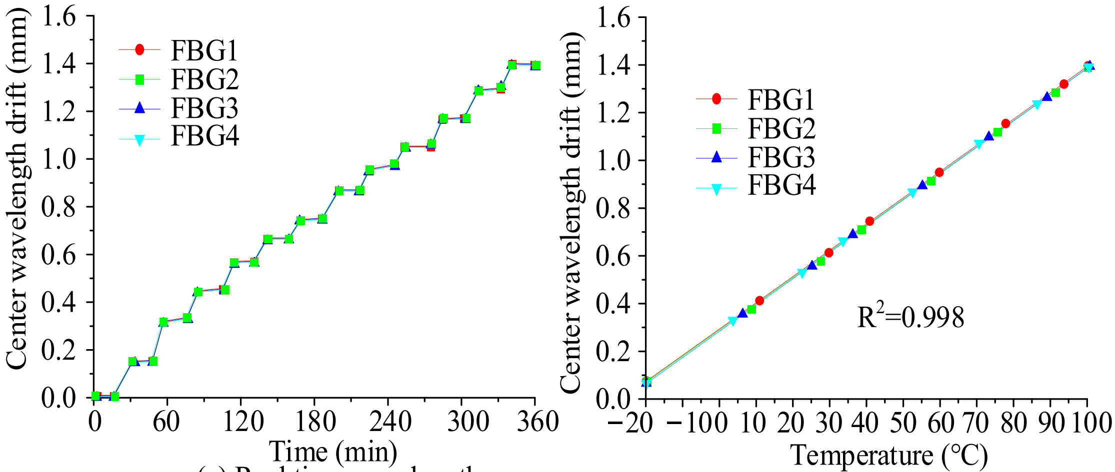

(a) Real time wavelength displacement curve of FBG sensor

(b) FBG sensor wavelength displacement fitting curve

Figure 6. Temperature calibration experiment

Figure 6 (a) shows the variation curve of the center wave of the FBG sensor with temperature displacement. As time increased, the center wavelength shift of the four sensors showed a step-like expansion, and the change curves of the four sensors were basically the same. In addition, an increase in temperature will increase the center wavelength shift of the FBG sensor. Figure 6 (b) shows the fitting curve of wavelength displacement for FBG sensors. The offset of the four sensors at different time periods was collected and fitted into a graph. The final fitting degree was 0.998. When the temperature increased by 1°C, the center wavelength increment of the sensor was controlled within the range of 10.5Pm, which met the temperature calibration requirements of the sensor. According to the fitting degree, the four sensors maintained high consistency and strong stability during the temperature change process. The slight variations in temperature sensitivity between the traditional FBG and the modified FBG are theoretically explained by specific technical differences. Specifically, the effective refractive index distribution is fundamentally altered by the non-uniform grating structure. Furthermore, the physical thermal expansion constraint of the silica fiber is modified by the specialized coupling interface. Consequently, the effective thermo-optic and thermal expansion coefficients are slightly shifted compared to bare traditional sensors, resulting in the observed sensitivity variations.

In addition, during the packaging process of FBG sensors, the optical fiber will be affected by the substrate medium, resulting in energy attenuation and larger monitoring errors. A temperature of 22℃ at room temperature is selected, and a 20g weight is suspended through a thin wire at the middle position of the four groups of FBG sensors. The weight is further increased every 25 seconds for a total of 3 loading cycles, and the wavelength displacement changes during the initial and three loading cycles are recorded, as shown in Figure 7.

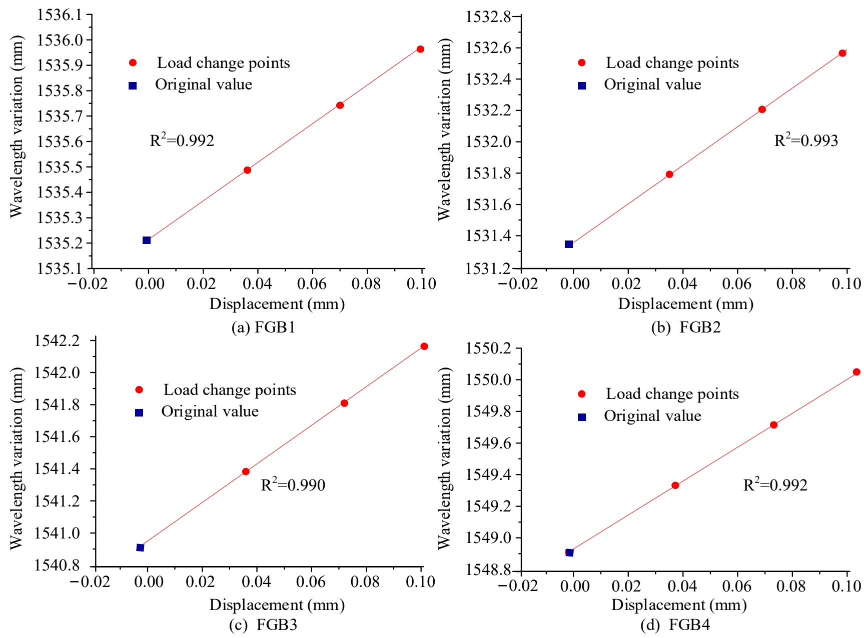

Figure 7. Overload calibration experiment

Figure 7 (a) shows the relationship between the wavelength and sensor displacement of sensor 1, where the blue direction represents the original wavelength value. After loading 20 into the sensor, the sensor displacement was 0.04mm, and the maximum was 0.10mm when applied for the third time. Influenced by the weight, the sensor wavelength increased from the initial 1535.2mm to 1536.0mm, with a displacement wavelength fit of 0.992 and a sensitivity of 12.448nm/mm. Figure 7 (b) shows the relationship between the wavelength and sensor displacement of sensor 2. As the loading weight increased, the wavelength gradually increased, with a fitting degree of 0.993 and a sensor sensitivity of 12.489nm/mm. This observed behavior is theoretically justified by the fundamental principles of strain-induced wavelength shift. Specifically, the increasing load induces an axial strain on the fiber. This mechanical tension physically elongates the grating period and alters the effective refractive index via the photo-elastic effect, thereby resulting in a proportional increase in the reflected center wavelength. In addition, the tests of sensor 3 and sensor 4 are shown in Figure 7 (c) and Figure 7 (d), with fitting degrees of 0.990 and 0.992, respectively. The sensitivity of the two sensors was 12.472nm/mm and 12.468nm/mm, respectively. The FBG sensor has effective linear fitting and excellent sensitivity, meeting the requirements of sensor accuracy design.

Monitoring of Dynamic Strain and Shear Deformation in Rock and Soil

The calibration experiment test results prove that the FBG sensor has effective temperature stability and accuracy. Therefore, the study compares the designed improved FBG sensor with traditional FBG sensors in geotechnical experiments. To comprehensively address the limitations of single soil type testing, further *in-situ* field validations are conducted across three typical geotechnical types: clay, silt, and gravel. Multiple experimental parameter conditions are configured, including variations in moisture content (5%, 15%, and 25%), dry density, and confining pressure. Furthermore, to rigorously evaluate the significance of these variables on monitoring accuracy, the Analysis of Variance (ANOVA) statistical method is introduced into the experimental design.

A temperature environment ranging from -20℃ to 100℃ is also set up inside the control box. Sensors are arranged on the surface of the rock and soil samples, and the strain of the rock and soil is tested at 1℃/min. The results are shown in Figure 8.

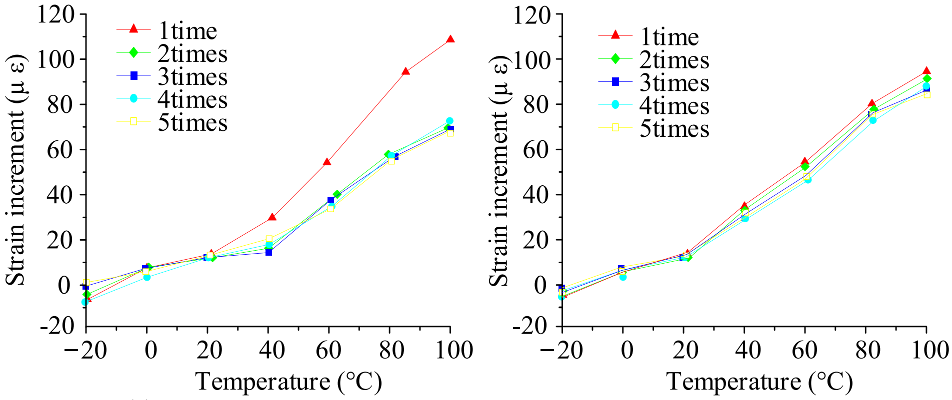

(a) FBG sensor measurement results

(b) Improve the measurement results of FBG sensors

Figure 8. Heating cycle experimental test

Figure 8 (a) shows the temperature-strain increment monitoring results of a traditional FBG sensor. According to the results, as the temperature gradually increased, the strain of the monitored sample increased. The higher the temperature, the greater the strain increment of the sample. In addition, after the first cycle of traditional FBG, the amplification of its monitoring curve significantly decreased, which was significantly different from the strain increment curve of the first round, indicating that the traditional FBG monitoring process was greatly affected by temperature, with a maximum monitoring error of 42.2με. Figure 8 (b) shows the temperature strain increment monitoring results of the improved FBG sensor. Similarly, as the temperature increased, the monitoring increment of the sensor gradually increased. As the number of cycles increased, the strain increment curve of the improved FBG sensor tended to fit. Further analysis revealed that the strain increment difference of the improved FBG in different times was small, and it was less affected by temperature. The monitoring error was within the range of 10.8με. The improved FBG sensor is less affected by temperature, and the dual-grating compensation method can effectively reduce temperature error interference.

To quantitatively evaluate the temperature compensation efficiency and analyze the residual temperature error, the proposed method is compared with standard temperature compensation techniques (such as the reference single-grating physical isolation method) under the aforementioned varying field conditions. The comprehensive statistical evaluation results are presented in Table 3.

Table 3. Quantitative evaluation of temperature compensation techniques under different geotechnical conditions

Soil Type	Parameter Condition	Compensation Technique	Compensation Efficiency (%)	Residual Temperature Error (με)	Statistical Significance (*p*-value)
Clay	Moisture 15%, High Density	Uncompensated FBG	-	45.2	<0.05
		Reference Isolation Method	75.4	11.1	<0.05
		Proposed Dual-Grating	92.1	3.5	<0.01
Silt	Moisture 5%, Medium Density	Uncompensated FBG	-	42.8	<0.05
		Reference Isolation Method	72.8	11.6	<0.05
		Proposed Dual-Grating	91.5	3.6	<0.01
Gravel	Moisture 25%, Low Density	Uncompensated FBG	-	48.5	<0.05
		Reference Isolation Method	70.2	14.4	<0.05
		Proposed Dual-Grating	89.8	4.9	<0.01

In Table 3, the proposed dual-grating method consistently achieved a compensation efficiency of approximately 90% across different soil types and complex field conditions, significantly outperforming the reference isolation method. The ANOVA results confirmed that the residual temperature error was suppressed to below 5.0 με, statistically proving that the proposed technique provides superior and robust temperature compensation regardless of geotechnical variations.

In addition, FBG sensors with depths of 5cm, 10cm, 15cm, and 25cm are buried at four different locations in the sample, with a spacing of 8cm. The strain monitoring effects of each sensor are set at different temperatures, as shown in Figure 9.

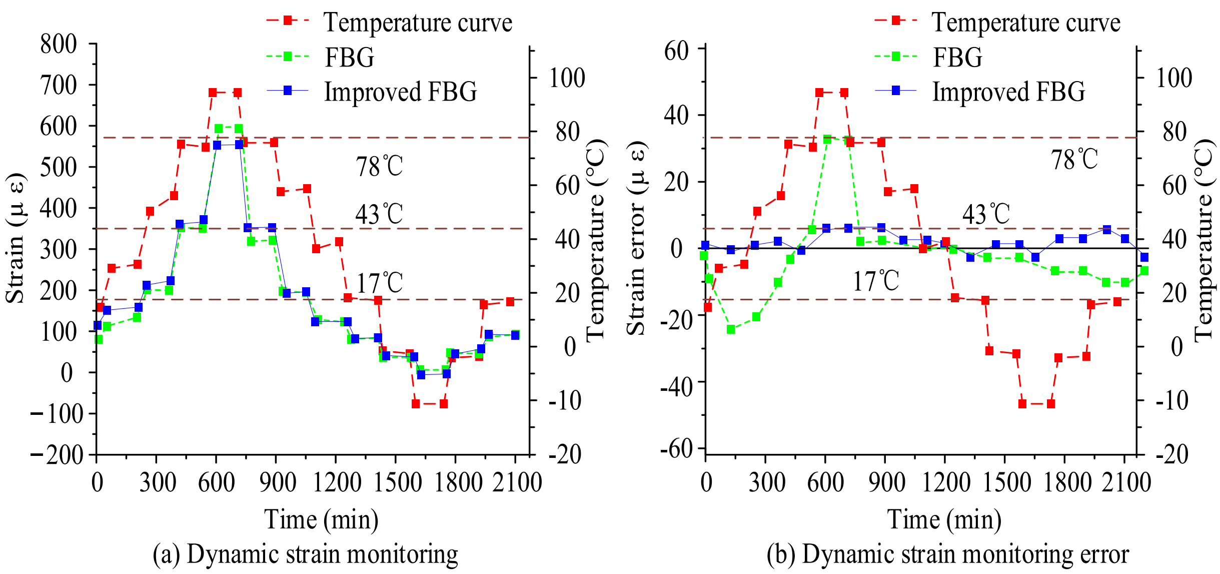

Figure 9. Dynamic strain monitoring results of different sensors

Figure 9 (a) shows the results of dynamic strain monitoring. There was a linear relationship between temperature and sample strain, that is, the larger the temperature value, the larger the sample strain value. In the temperature range of 17°C, 43°C, and 78°C, both sensors monitored sample amplification exceeding 100με, indicating that temperature had a significant impact on rock strain. The higher the temperature, the greater the internal strain. Figure 9 (b) shows the results of dynamic strain monitoring error. The strain monitoring error of the improved FBG sensor was controlled at 7.8με, while the maximum error of the FBG sensor was 50.2με. The improved FBG sensor performs better in strain monitoring. In addition, the study sets the room temperature to 22°C and obtains the shear deformation results of the samples based on strain monitoring. This reference temperature is maintained to isolate the shear deformation characteristics from complex thermal-mechanical coupling effects in the soil mass. Based on this stable baseline, the monitoring precision of the improved FBG sensor is strictly evaluated, while any potential temperature-induced wavelength drift is independently addressed by the dual-grating compensation method, as shown in Figure 10.

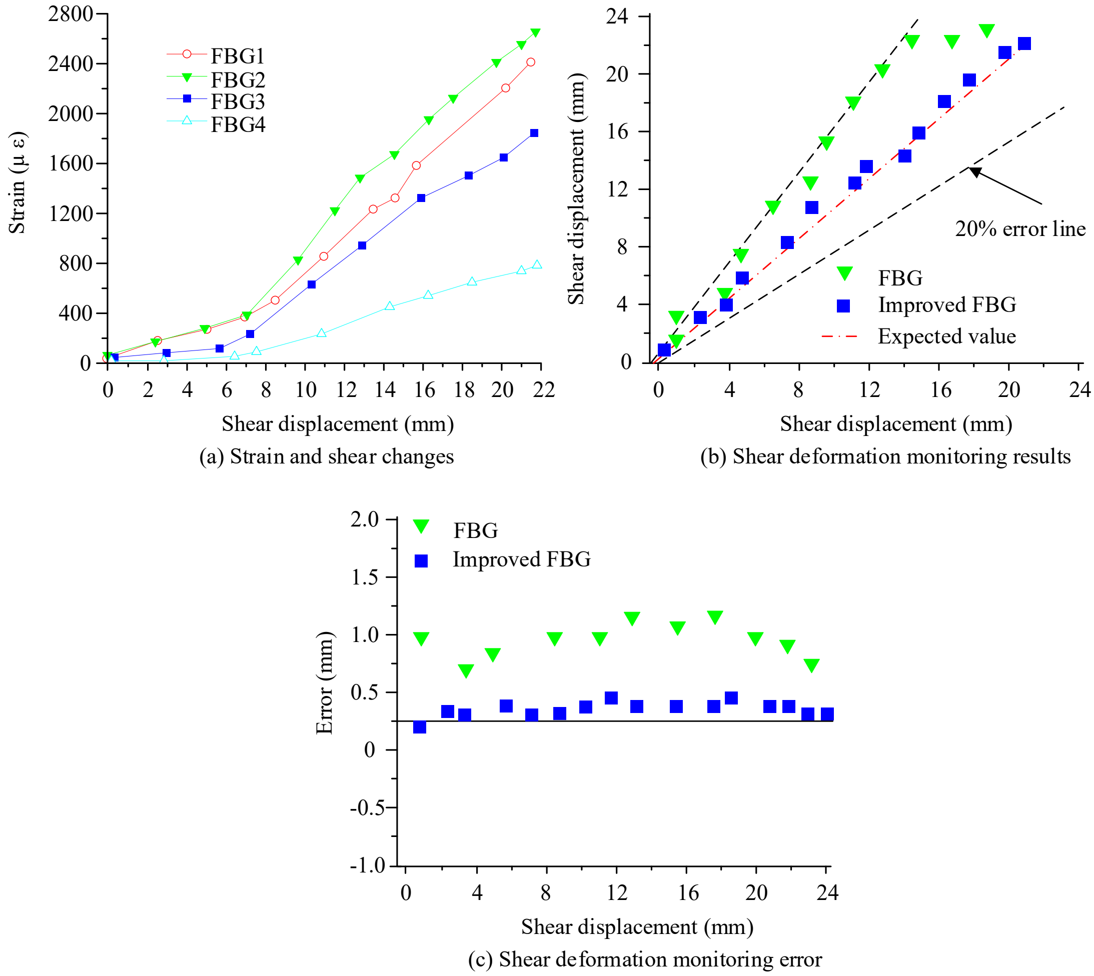

Figure 10. Monitoring results of rock shear deformation

Figure 10 (a) shows the relationship between strain and shear force under improved FBG sensor. According to the test, strain is positively correlated with shear displacement, and the greater the strain, the greater the shear displacement of the material. When the strain was 801, sensor 4 monitored a shear displacement of 22mm. Figure 10 (b) shows the shear deformation monitoring result. The red dashed line represents the expected value. Based on the test results, the improved FBG sensor was closer to the actual shear displacement, while traditional FBG monitoring had larger fluctuations. Figure 10 (c) shows the results of shear deformation monitoring error. The maximum shear deformation monitoring error of the improved FBG was 0.47mm, while the maximum error of the traditional FBG sensor was 1.42mm. The improved FBG has better accuracy in rock and soil shear-strain monitoring.

To justify the utilization of the CNN for the highly nonlinear problem scale, a 5-fold cross-validation strategy is employed to evaluate the model performance before the final comprehensive statistics. The improved CNN is systematically compared with simpler and alternative models, including Multiple Linear Regression (MLR), Artificial Neural Network (ANN), and Long Short-Term Memory (LSTM) networks. The performance metrics, including Root Mean Square Error (RMSE), Mean Absolute Error (MAE), and Coefficient of Determination (R^2), are summarized in Figure 11.

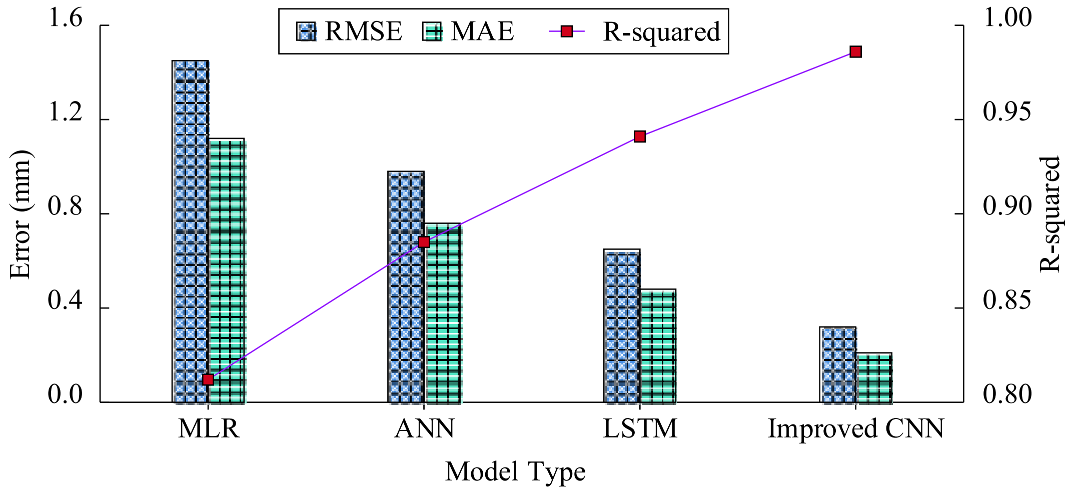

Figure 11. Performance comparison of different prediction models

From Figure 11, simpler models, such as MLR and ANN, struggle to accurately capture the complex spatial coupling of geotechnical deformation. Although the LSTM model performed adequately, the improved CNN achieved the highest R^2 (0.986) and the lowest error metrics. This explicitly justifies that the spatial attention-enhanced CNN is highly suitable and robust for the targeted problem scale, validating its structural advantages for the subsequent comprehensive shear deformation monitoring.

Finally, two orthogonal FBG sensing fibers are buried in the middle of the sand sample at a depth of 50mm to statistically analyze the shear deformation parameters of the rock and soil. A state-of-the-art FBG demodulation method based on ML (Bi-LSTM) is used as a comparative approach. The monitoring results are shown in Table 4.

Table 4. Comprehensive monitoring results of changes in rock and soil shear stress

Actual shear displacement (mm)	Cumulative strain (μ ε)	Fiber elongation (mm)	FBG shear monitoring		Improved FBG shear monitoring		Improved CNN correction value		State-of-the-art ML monitoring	
			Monitoring value (mm)	Deviation (mm)	Monitoring value (mm)	Deviation (mm)	Monitoring value (mm)	Deviation (mm)	Monitoring value (mm)	Deviation (mm)
2.02	80.2	0.038	2.56	0.54	2.35	0.33	2.15	0.13	2.25	0.23
4.23	100.5	0.054	6.48	2.25	5.68	1.45	4.58	0.35	5.08	0.85
6.15	385.5	0.082	7.45	1.30	6.85	0.70	6.28	0.13	6.55	0.40
8.05	410.5	0.157	9.85	1.80	9.25	1.20	8.45	0.40	8.80	0.75
10.03	807.6	0.257	11.25	1.22	10.25	0.22	10.25	0.22	10.25	0.22
12.08	1205.8	0.391	13.85	1.77	12.85	0.77	12.35	0.27	12.58	0.50
14.05	1618.7	0.489	16.58	2.53	15.58	1.53	14.58	0.53	15.05	1.00
16.05	1983.8	0.576	19.45	3.40	17.85	1.80	16.29	0.24	17.00	0.95
18.06	2256.8	0.668	19.85	1.79	18.95	0.89	18.56	0.50	18.76	0.70
20.01	2415.8	0.775	21.86	1.85	21.28	1.27	20.68	0.67	20.96	0.95
22.02	2726.8	0.854	24.58	2.56	23.85	1.83	22.86	0.84	23.32	1.30
24.25	3025.5	0.958	27.28	3.03	26.85	2.60	24.95	0.70	26.10	1.85

Table 4 shows the comprehensive monitoring results of rock and soil shear deformation. The greater the shear displacement, the greater the fiber elongation. When the actual shear displacement increased from 2.02mm to 6.15mm, the corresponding fiber elongation increased from 0.038mm to 0.082 mm. In addition, the improved FBG sensor for shear monitoring was significantly better. For example, when the actual shear displacement was 22.02, the traditional FBG monitoring value was 24.58mm, with a maximum deviation of 2.56mm, while the improved FBG monitoring value was 23.85mm, with an error of 1.83mm. The improved FBG sensor had higher monitoring accuracy. However, the improved FBG sensor in actual monitoring is still susceptible to the influence of spatial offset and strain modeling. Therefore, the study uses an improved CNN to optimize the strain offset step size. The maximum error of rock and soil shear deformation after optimizing the improved CNN was 0.84mm. In contrast, the maximum errors for the traditional FBG, the improved FBG, and the state-of-the-art ML-based method were 3.03mm, 2.60mm, and 1.85mm, respectively. This comparison confirms that the proposed method possesses superior accuracy in monitoring scenarios.

To provide rigorous validation of the internal relationship between sensed wavelength shift, strain, and resultant shear deformation, a parameter conversion consistency test is performed. The results are summarized in Table 5.

Table 5. Validation of the relationship between sensing parameters and shear deformation

Group	Wavelength Shift (pm)	Calculated Strain (με)	Calculated Deformation (mm)	Measured Deformation (mm)	Relative Error (%)
1	99.4	80.2	2.15	2.02	6.44
2	478	385.5	6.28	6.15	2.11
3	1001.4	807.6	10.25	10.03	2.19
4	2509.6	2024.1	18.56	18.06	2.77
5	3381.2	2726.8	22.86	22.02	3.81

The results in Table 5 demonstrated that the conversion logic from wavelength shift to shear deformation maintained high physical consistency across various loading conditions. The small relative errors confirm that the research successfully validates the theoretical framework through experimental data, ensuring the reliability of the monitoring system in complex geotechnical environments.

To strictly quantify the reliability of the monitoring system, an error propagation analysis is conducted to evaluate how primary input uncertainties affect the final shear deformation output. The error propagation results are shown in Table 6.

Table 6. Error propagation analysis for shear deformation monitoring

Error Source	Input Uncertainty	Propagated Strain Error (με)	Propagated Shear Error (mm)
Demodulator resolution	±0.1 pm	±0.08	±0.02
Temperature fluctuation	±0.5 °C	±5.20	±0.15
System noise	±0.2 pm	±0.16	±0.05
Cumulative uncertainty	-	±5.44	±0.22

In Table 6, temperature fluctuation was the dominant source of propagated error (±0.15 mm). However, the cumulative shear deformation uncertainty was constrained to ±0.22 mm. This base system uncertainty is efficiently managed by the structural design and is significantly lower than the ultimate monitoring errors, verifying the robustness of the improved CNN model in mitigating propagated uncertainties from complex environmental inputs.

CONCLUSION

A sensor based on improved FBG was proposed to address the stress parameter monitoring in geotechnical engineering being constrained by complex environments. The study first constructed an FBG sensor model based on the coupling mode theory, analyzed the non-uniform grid spacing spectral characteristics using the segmented transfer matrix method, and established an improved FBG sensor monitoring system. Secondly, the study introduced improved CNN and attention mechanism to optimize the strain offset step size. In the experiment, the calibration results of the FBG sensor showed that the fitting degree of the sensor between wavelength displacement and temperature was 0.998, indicating strong stability. In the overload verification experiment, the sensitivity of sensor 3 and sensor 4 was 12.472 nm/mm and 12.468 nm/mm, respectively, meeting the accuracy requirements. In dynamic strain monitoring of rock and soil, the improved FBG sensor had a monitoring error controlled within 7.8με, which was better than that of the traditional sensor (50.2με). In shear deformation monitoring, the maximum monitoring error of the improved FBG sensor was 0.47mm, which was better than that of the traditional sensor (1.42mm). In comprehensive monitoring of rock and soil shear deformation, after optimizing the improved CNN, the shear deformation error was controlled within 0.84mm, significantly lower than that of the traditional FBG sensor (3.03mm) and the improved FBG sensor (2.60mm). The improved FBG sensor has excellent application effects in dynamic strain and shear deformation of rock and soil. However, specific limitations and challenges encountered during the analysis are explicitly acknowledged by the research. A homogeneous soil density within each test layer is assumed, while secondary parameters, such as long-term soil creep and chemical corrosion, are simplified or neglected. Consequently, unmodeled geotechnical variations and long-term environmental degradation are identified as potential sources of uncertainty in the system. Future research will further improve sensors and increase humidity scene monitoring to alleviate these uncertainties and enhance adaptability to different complex scenarios.

Data Availability

The data that supports the findings of this study is available from the corresponding author upon reasonable request.

REFERENCES

Abdulraheem, M.I., Xiong, Y., & Zhang, W. (2024). Recent applications of fiber Bragg grating sensors in humidity and water content detection in agriculture: A comprehensive review of development, challenges, and future trends. *International Journal of Precision Engineering and Manufacturing, 25*(7), 1499-1524. https://doi.org/10.1007/s12541-024-01015-6

Adibnia, E., Ghadrdan, M., & Mansouri-Birjandi, M.A. (2023). Prediction of fiber Bragg gratings characteristics from its design parameters using deep learning. *International Journal of Optics and Photonics, 17*(2), 165-174. https://doi.org/10.61186/ijop.17.2.165

Alias, M.A., Ahmad, H., & Thambiratnam, K. (2024). Performance comparison of a 3-D printed fiber Bragg grating (FBG) load cell sensor based on the influence of different infill density and pattern. *IEEE Sensors Journal, 24*(8), 12400-12412. https://doi.org/10.1109/JSEN.2024.3372145

Al-Mamoori, S.K., Karkush, M., Al-Baghdadi, W.H., & Al-Rumaithi, A.A. (2025). Spatial variation of shallow soil bearing capacity using SPT data and MATLAB analysis. *Civil Engineering Journal, 11*(11), 4745-4761. https://doi.org/10.28991/CEJ-2025-011-11-017

Chen, C. W., Balliu, E., & Talbot, L. (2024). Calibration of a high-resolution slow-light fiber-Bragg-grating sensor for temperature measurements of laser-cooled fibers. *Journal of Lightwave Technology, 42*(20), 7391-7397. https://doi.org/10.1109/JLT.2024.3416867

Choi, B.K., Kim, J.S., Ahn, S., & Yoon, S. (2024). Simultaneous temperature and strain measurement in fiber Bragg grating via wavelength-swept laser and machine learning. *IEEE Sensors Journal, 24*(17), 27516-27524. https://doi.org/10.1109/JSEN.2024.34 29366

Dostovalov, A., Kokhanovskiy, A., & Golikov, E. (2024). Fiber Bragg grating inscription assisted by a spatial light modulator. *Optics Letters, 49*(4), 1077-1080. https://doi.org/10.1364/OL.514896

Gul, B., & Ahmad, F. (2023). Fiber Bragg grating as a sole dispersion compensation unit for a long haul optical link. *Photonic Network Communications, 46*(2), 68-77. https://doi.org/10.1007/s11107-023-01001-4

Han, H., Shi, B., Zhang, C.C., Sang, H., Huang, X., & Wei, G. (2023). Application of ultra-weak FBG technology in real-time monitoring of landslide shear displacement. *Acta Geotechnica, 18*(5), 2585-2601. https://doi.org/10.1007/s11440-022-01742-y

Hebbi, C., & Mamatha, H. (2023). Comprehensive dataset building and recognition of isolated handwritten Kannada characters using machine learning models. *Artificial Intelligence and Applications, 1*(3), 179-190. https://doi.org/10.47852/bonviewAIA3202624

Hu, B., Zhang, X., Meng, Y., Li, J., Wang, Z., & Ding, W. (2023). Research on application of fiber Bragg grating seepage pressure sensor in soil test. *IEEE Sensors Journal, 23*(15), 16840-16850. https://doi.org/10.1109/JSEN..2023.3279490

Ioannou, A., & Kalli, K. (2023). Femtosecond laser inscribed fiber Bragg gratings based on precise spatial apodization. *Optics Letters, 48*(7), 1826-1829. https://doi.org/10.1364/OL.485369

Karkush, M., & Ali, S. D. (2025). Durability of gypseous soil stabilized with nano-silica under environmental conditions. *Jordan Journal of Civil Engineering, 19*(1), 164-164. https://doi.org/10.14525/JJCE.v19i1.12

Karkush, M.O., Al-Murshedi, A.D., & Karim, H.H. (2020). Investigation of the impacts of nano-clay on the collapse potential and geotechnical properties of gypseous soils. *Jordan Journal of Civil Engineering, 14*(4), 537-547. https://doi.org/10.13140/RG.2.2.35390.73282

Karkush, M.O., Sabaa, M.R., Salman, A.D., & Al-Rumaithi, A. (2022). Prediction of bearing capacity of driven piles for Basrah governorate using SPT and MATLAB. *Journal of the Mechanical Behavior of Materials, 31*(1), 39-51. https://doi.org/10.1515/jmbm-2022-0005

Kok, S.P., Go, Y.I., Wang, X., & Wong, M.L. (2024). Advances in fiber Bragg grating (FBG) sensing: A review of conventional and new approaches and novel sensing materials in harsh and emerging industrial sensing. *IEEE Sensors Journal, 24*(19), 29485-29505. https://doi.org/10.1109/JSEN.2024.3434351

Li, C., Tong, X., Huang, W., & Wang, Y. (2024). Development of a fast response, high accuracy, and miniaturized fiber Bragg grating (FBG) sensor for fluid temperature measurement. *IEEE Sensors Journal, 24*(6), 8746-8753. https://doi.org/10.1109/JSEN.2024.3358386

Liu, D., Cai, Z., & Li, B. (2023). Simultaneous measurement of humidity and temperature based on fiber-tip microcantilever cascaded with fiber Bragg grating. *Optics Express, 31*(5), 8738-8747. https://doi.org/10.1364/OE.479340

Prathap, P.B., & Saara, K. (2024). Quantifying efficacy of the fiber Bragg grating sensors in medical applications: A survey. *Journal of Optics, 53*(5), 4180-4201. https://doi.org/10.1007/s12596-023-01480-8

Presti, D.L., Massaroni, C., & Bianchi, D. (2023). A wearable flower-shaped sensor based on fiber Bragg grating technology for *in vivo* plant growth monitoring. *IEEE Sensors Journal, 23*(8), 8416-8425. https://doi.org/10.1109/JSEN.2023.3253782

Salman, A.D., Shimran Khadim, S., Karkush, M., & Al-Rumaithi, A. (2024). Production of maps for bearing capacity of the shallow foundation in Baghdad city using SPTs and MATLAB software. *IOP Conference Series: Earth and Environmental Science, 1374*(1), Article 012023. https://doi.org/10.1088/1755-1315/1374/1/012023

Sun, M., Liu, J., Liu, J., Zheng, X., Li, X., & Guo, J. (2025). Development and in situ application of actively heated fiber Bragg grating cable for soil water content measurement. *Journal of Rock Mechanics and Geotechnical Engineering, 17*(7), 4579-4590. https://doi.org/10.1016/j.jrmge.2024.09.033

Wang, D., Zhu, H., Zhou, G., & Yu, W. (2024). Monitoring shear deformation of sliding zone via fiber Bragg grating and particle image velocimetry. *Journal of Rock Mechanics and Geotechnical Engineering, 16*(1), 231-241. https://doi.org/10.1016/j.jrmge.2023.03.007

Yamaguchi, T., Kawashima, H., Matsuda, H., & Shinoda, Y. (2023). Experimental demonstration of peak wavelength measurement of multiplexing fiber Bragg gratings using convolutional neural network. *IEEE Sensors Journal, 23*(9), 9343-9352. https://doi.org/10.1109/JSEN.2023.3262494

Zhang, M., Zhu, H., Yang, J., & Qiu, C. (2023). Experimental study of a 3D printed geogrid embedded with FBG sensor for reinforcement of subgrade with underlying cave. *Geotextiles and Geomembranes, 51*(5), 81-92. https://doi.org/10.1016/j.geotexmem.2023.05.001

Zhao, J., Dong, W., Hinds, T., Li, Y., & Splain, Z. (2023). Embedded fiber Bragg grating (FBG) sensors fabricated by ultrasonic additive manufacturing for high-frequency dynamic strain measurements. *IEEE Sensors Journal, 24*(3), 2853-2862. https://doi.org/10.1109/JSEN.2023.3343604